Tribology International 219 (2026) 111789

Contents lists available at ScienceDirect

Tribology International

journal homepage: www.elsevier.com/locate/triboint

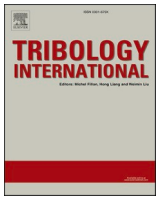

Full length article

Failure assessment of crack propagation in as-built LPBF 17–4PH stainless steel under rolling contact fatigue

Nicola Zani [a,*], Candida Petrogalli [a], Kang Shu [b], Angelo Mazzù [a], Giorgio Donzella [a]

[a] Department of Mechanical and Industrial Engineering, University of Brescia, Via Branze, 38, Brescia 25123, Italy
[b] College of Mechanical Engineering, Hunan Institute of Science and Technology, Xueyuan Road, 439, Yueyang 414006, China

ARTICLE INFO

Keywords:
Rolling Contact Fatigue
Crack Propagation
Laser Powder Bed Fusion
Failure Assessment Diagram

ABSTRACT

This work presents an integrated experimental–numerical study on the rolling contact fatigue (RCF) behaviour of as-built Laser Powder Bed Fused (L-PBF) 17–4PH stainless steel lubricated with water and oil. Controlled twin-disc tests, finite element analyses and modelling were combined to clarify the influence of lubrication on crack initiation and propagation mechanisms. Water-based lubrication promoted accelerated crack growth due to hydraulic pressurization and enhanced shear stresses, while oil lubrication provided a stable elastohydrodynamic separation, delaying crack initiation and mitigating branching. A novel predictive framework was formulated by incorporating elastohydrodynamic similarity parameters into a generalized crack-growth law, enabling the quantification of mechanical–tribological coupling effects. The proposed model exhibited strong agreement with experimental data ($R^2 = 0.75$, RMSE = 0.195), confirming the synergistic contribution of stress intensity and viscous dissipation in controlling fatigue damage evolution. Furthermore, the Failure Assessment Diagram (FAD) methodology was extended to account for finite-life and lubrication effects, successfully delineating the transition from crack arrest to propagation across pressure regimes. The developed approach provides a unified, physically consistent basis for assessing lubrication-dependent fatigue performance in additively manufactured steels, offering enhanced predictive capability for RCF design of AM components.

1. Introduction

A comprehensive understanding of Rolling Contact Fatigue (RCF) is essential in mechanical engineering, as it governs the reliability and lifespan of virtually all the rotating components subjected to cyclic contact loading. Bearings and gears, in particular, operate under stresses frequently reaching gigapascal levels, where repeated subsurface shear leads to crack initiation, pitting, and eventually spalling or catastrophic failure. In rolling element bearings, RCF is widely recognized as the predominant failure mechanism, dictating service intervals, influencing operational downtime, and determining the overall cost of maintenance and replacement.

Among the materials employed in rolling contact applications, 17–4PH precipitation-hardening stainless steel is widely used in mechanical components requiring a combination of high strength, good fatigue resistance, and corrosion resistance. Typical applications include gears, rolling element bearings, shafts, and transmission components operating in aggressive or water-contaminated environments, such as aerospace actuation systems, marine and offshore equipment, pumps, and industrial gearboxes. In these applications, rolling or rolling–sliding contact conditions are frequently encountered, and rolling contact fatigue represents a primary damage mechanism governing service life.

Modern engineering trends, characterized by higher load densities, thinner lubrication films, and increasingly refined surface finishes, have amplified the susceptibility of components to RCF damage. The shift towards compact, energy-efficient machinery has raised the contact stress levels while simultaneously reducing the lubricant film thickness, making even minor surface imperfections critical to fatigue life. Consequently, the accurate prediction and mitigation of RCF have become central to modern tribological design. Despite decades of research, predictive tools and in-situ diagnostic methods often fall short of the complexity observed in real-world conditions, emphasizing the need for multiscale, physics-based frameworks capable of linking material response to operating parameters.

In this context, the Failure Assessment Diagram (FAD) approach developed by Donzella et al. [1,2] has emerged as a unified tool to assess the stability of cracks under rolling contact conditions. The original formulation, based on Murakami's defect theory [3] and the El-Haddad

* Corresponding author.
E-mail address: nicola.zani@unibs.it (N. Zani).

https://doi.org/10.1016/j.triboint.2026.111789
Received 18 November 2025; Received in revised form 21 January 2026; Accepted 2 February 2026
Available online 5 February 2026

short-crack model [4], enabled the transition from non-propagating to propagating states to be represented in terms of defect size and Hertzian pressure. Defects and inclusions were treated as equivalent cracks, and their propagation tendency was evaluated by comparing the applied stress intensity factor range with the short-crack threshold. This representation allowed the safe, finite, and ratcheting domains of fatigue behaviour to be clearly identified. Subsequent developments incorporated experimental data on gear steels, showing that oxides and sulphides serve as preferential crack nuclei and that extreme-value statistical estimation of inclusion size could be integrated into the FAD to achieve quantitative life predictions [2,5]. Later extensions introduced iso-life curves, bridging infinite-life design and finite-life fatigue regimes, and accounting for surface-hardened steels with hardness gradients typical of carburized and nitrided components [6].

Parallel to these theoretical developments, research into additively manufactured (AM) metals has expanded rapidly, driven by the need for lightweight, complex, and functionally optimized components. The layer-wise solidification process intrinsic to AM introduces unique microstructural and defect-related challenges, such as porosity, lack-of-fusion flaws, melt-pool boundaries, and strong residual stress fields, that profoundly affect fatigue performance [7–9]. In martensitic stainless steels such as 17–4 PH, the as-built condition exhibits heterogeneous microstructures with δ-ferrite remnants, unmelted particles, and local compositional segregation, all of which reduce fatigue strength compared with conventionally processed counterparts [10–12]. Murr et al. [10] and Akita et al. [11] demonstrated that fatigue cracks in selective laser melted (SLM) 17–4 PH preferentially initiate at small voids or inclusions (<50 μm), with frequent branching and deflection caused by the complex thermal microstructure. Yadollahi et al. [12] and Nezhadfar et al. [13] further showed that, after suitable heat treatments such as H900 or CA-H900, AM 17–4 PH can achieve crack-growth rates and Paris-regime behaviour comparable to wrought steels, although anisotropy and build orientation still influence near-threshold propagation.

These findings underscore that the fatigue response of AM alloys cannot be dissociated from their hierarchical microstructure. Becker et al. [8] and Liu et al. [9] reviewed how melt-pool boundaries, residual stresses, and local phase transformations combine to produce fatigue mechanisms distinct from those of wrought metals, often dominated by internal defect-driven initiation rather than surface slip banding. Meanwhile, foundational works by Herzog et al. [7] established the metallurgical basis of AM processes, correlating the extreme thermal gradients and solidification kinetics to cellular and columnar grain morphologies, while Coors et al. [14] demonstrated the practical potential of stainless AM materials for bearing applications when proper heat treatment and post-processing are employed. More recent investigations on AM gears, both in 17–4 PH [15] and 316 L stainless steel [16], have revealed that layer thickness, surface finishing, and lubrication strongly modulate wear and contact fatigue, confirming the intricate interplay between surface integrity and load transmission.

For AM components operating under rolling or mixed-sliding contact, lubrication conditions add a further dimension to the fatigue problem. Zani et al. [17] demonstrated that in L-PBF 17–4 PH, oil lubrication delays crack initiation and restricts branching, whereas water promotes hydraulic pressurization within surface pits, accelerating propagation and shelling. Morales et al. [18] subsequently introduced the concept of a surface risk parameter, quantifying the ratio of near-surface to total stress integrals, which enables the discrimination between surface-driven micropitting and subsurface spalling modes under given operating conditions. The investigation was intentionally conducted on as-built specimens to establish a conservative baseline for lubrication-dependent RCF behaviour.

On these bases, the present study aims to extend the FAD methodology by incorporating elastohydrodynamic (EHL) descriptors, thereby enabling a unified prediction framework for lubrication-dependent fatigue life in AM 17–4 PH steel. The paper first reviews the experimental characterization of as-built specimens under controlled lubrication regimes, establishing the baseline RCF behaviour. It then introduces a coupled numerical–analytical approach that integrates finite element simulations, crack growth modelling, and an EHL-sensitive extension of the FAD. The ultimate objective is to achieve a mechanistic, physically informed prediction of rolling contact fatigue in AM stainless steels.

2. Experimental basis

2.1. Test method

The following section provides a concise overview of the experimental results previously reported by Zani et al. [17], which constitute the basis for the numerical and analytical developments presented in this work. In that study, the rolling contact fatigue (RCF) behaviour of as-built L-PBF 17–4PH stainless steel was systematically investigated under controlled lubrication regimes using a bi-disc test rig (Fig. 1**a**).

The specimens of 17–4PH stainless steel (Fig. 1a) were manufactured in the as-built condition by Laser Powder Bed Fusion (L-PBF) using a ProX® DMP 100 system under an inert nitrogen atmosphere. The optimized process parameters (laser power: 100 W, scanning speed: 300 mm/s, hatch spacing: 50 μm, and layer thickness: 30 μm) ensured a relative density above 99.9 %. The feedstock was LaserForm® 17–4PH (A) powder, compliant with ASTM F899 and UNS S17400 standards, and the resulting microstructure exhibited the typical mosaic morphology with retained austenite stabilized by nitrogen. Table 1 and Table 2 shows the chemical composition of the powder and the mechanical properties, respectively.

Microstructure was identified with Kalling chemical etching on the rolling plane (5 g of $CuCl_2$, 100 ml of ethanol and 100 ml of HCl for 30 s at room temperature) using a 3D microscopic system (KEYENCE VHX-5000, Japan) and scanning electron microscope (SEM, Phenom Pro-SE, Netherlands). The as-built L-PBF 17–4 PH stainless steel displayed a complex and heterogeneous microstructure predominantly composed

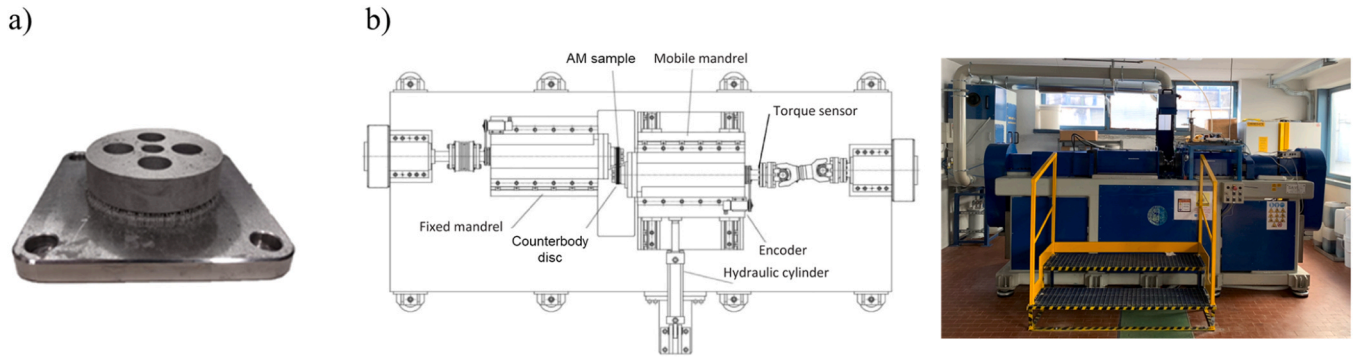

Fig. 1. a) AM printed sample; b) Bi-disc test bench and technical diagram of the bench.

Table 1
Chemical composition of the powder [17].

Element	Fe	C	Mn	S	P	Cr	Si	Ni
Weight [%]	Bal.	< 0.07	< 1.00	< 0.030	< 0.040	15.00 – 17.50	< 1.00	3.00 – 5.00

Table 2
Mechanical properties of as-built 17–4PH [17].

Ultimate Strength [MPa] ASTM E8M	Yield Strength [MPa] ASTM E8M	Elongation at break [%] ASTM E8M	Brinel hardness ASTM E10
1100	900	19	300

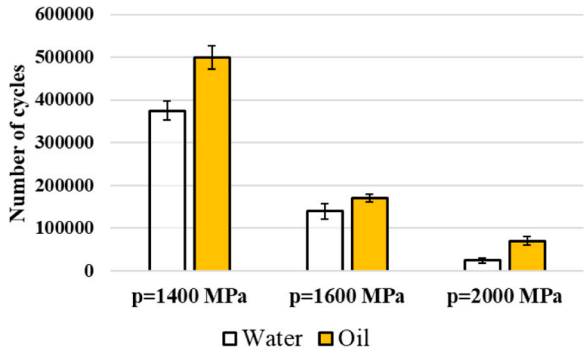

Fig. 2. Cycles to initial surface damage under oil and water lubrication.

of columnar δ-ferrite grains, with small regions of martensite and retained austenite. Energy-dispersive spectroscopy revealed local Cu-rich segregations, associated with incomplete diffusion and rapid solidification during the additive manufacturing process. In the reference experimental study, the surface roughness was measured on each specimen prior to testing in order to verify comparable initial conditions, yielding an average initial value of $R_a = 19 \pm 3$ μm for the as-built LPBF 17–4PH samples.

The samples were 60 mm in diameter and 15 mm in thickness. Rolling contact fatigue (RCF) tests were carried out on the test rig (Fig. 1b) described in [19], under pure rolling conditions at nominal Hertzian pressures of 1400, 1600, and 2000 MPa, corresponding to 12 kN, 15.6 kN and 24.5 kN, respectively. Two lubrication regimes were examined: the commercial oil Mobilgear 600 XP 150 and water–glycol with a flow rate of 6×10^{-3} m^3/s. In the previous study, failure was defined as the occurrence of catastrophic spalling, whereas in the present work the number of cycles to failure was determined from the first detectable damage signal recorded by the accelerometer mounted on the test bench. Specifically, failure was identified as the number of cycles corresponding to a 25 % increase in the stable acceleration signal of the tested 17–4PH specimen with respect to the initial baseline [20,21]. Fig. 2 reports the number of cycles corresponding to this first measurable rise in acceleration, marking the onset of surface damage in the 17–4PH specimen.

2.2. Test results

Under cyclic loading, surface pitting consistently appeared as the initial degradation stage, acting as a stress concentrator that promoted fatigue crack nucleation. Once formed, cracks propagated mainly across the microstructure, without following paths or clearly guided by specific microstructural features. This indicates that local stress concentrations and cyclic shear stresses governed crack evolution, outweighing any anisotropy introduced by the L-PBF process. Fig. 3 summarizes the main damage features observed: spalling, surface cracking and shelling. Surface cracks represent a critical transition stage in the fatigue process; while their nucleation is sensitive to the microstructural features and surface asperities, their subsequent development into long cracks is primarily driven by the stress field. Spalling was mainly associated with pit evolution and localized material removal at medium to high contact pressures, where higher Hertzian stresses promoted crack propagation from the spalled region. Lubrication played a key role in determining both morphology and severity of surface crack damage. Under water lubrication, cracks were deeper, more branched, and highly interconnected, consistent with hydraulic pressurization effects due to fluid entrapment within the crack network. This mechanism enhanced crack opening, accelerated branching and frequently led to shelling and material detachment. Conversely, oil lubrication provided a more protective regime, delaying crack initiation and limiting vertical crack growth. Cracks in oil-lubricated samples were typically narrower, less branched and propagated laterally along the rolling plane, reflecting the stabilizing effect of the oil film in reducing asperity contact and local plastic deformation. In several cases, debris particles were found within crack cavities, modifying local stress fields and influencing crack propagation. Depending on their morphology and composition, these particles either delayed crack advance by partially closing the crack tip or promoted secondary cracking by acting as stress concentrators. From a rheological perspective, the markedly different viscosities of the two lubricants strongly influenced the film-forming capability at the contact interface. The water–glycol mixture, characterized by a viscosity one to two orders of magnitude lower than that of the reference oil, was unable to sustain a stable lubrication film under the high Hertzian pressures. This condition favoured direct asperity contact and hydraulic fluid penetration into surface cracks. This explains the enhanced crack branching and hydraulic pressurization effects observed in the water-lubricated tests. Conversely, the higher-viscosity oil maintained a more continuous film, effectively separating the surfaces and attenuating cyclic shear stresses at surface asperities. This reduced the amplitude of surface traction and plastic strain accumulation, delaying both pitting and crack initiation. These results are consistent with the friction trends reported in the previous study, where oil yielded a steady-state coefficient around 0.027, roughly double that measured for water (0.013), confirming the thicker and more stable lubricant film provided by the higher-viscosity medium. A comprehensive cross-sectional microstructural analysis and surface morphological damage for all load and lubrication conditions is reported in [17] and is not repeated here to avoid redundancy.

Statistical analysis of the cracks reveals a distinct correlation between the lubricant type and the resulting damage morphology (Fig. 4). Water-lubricated specimens exhibit a significant acceleration in crack growth, with lengths exceeding 1100 μm and depths reaching up to 550 μm, likely driven by hydraulic pressurization within the crack network. In contrast, oil lubrication provides a protective effect, effectively limiting vertical penetration to depths primarily below 120 μm and favouring a more stable lateral propagation along the rolling plane. Interestingly, the most extensive crack growth occurs at lower Hertzian pressures (1400–1600 MPa), where the higher number of cycles to failure allows for more prolonged physical propagation compared to the rapid failures observed at 2000 MPa.

3. Crack propagation rate

Based on the experimental evidence of surface-initiated cracking, this section quantifies the crack propagation behaviour through finite element simulations, elucidating the relationship between lubrication regime, stress intensity evolution, and fatigue damage progression. One specimen was examined for each load–lubrication condition, and only primary, non-branched surface cracks were included in the assessment

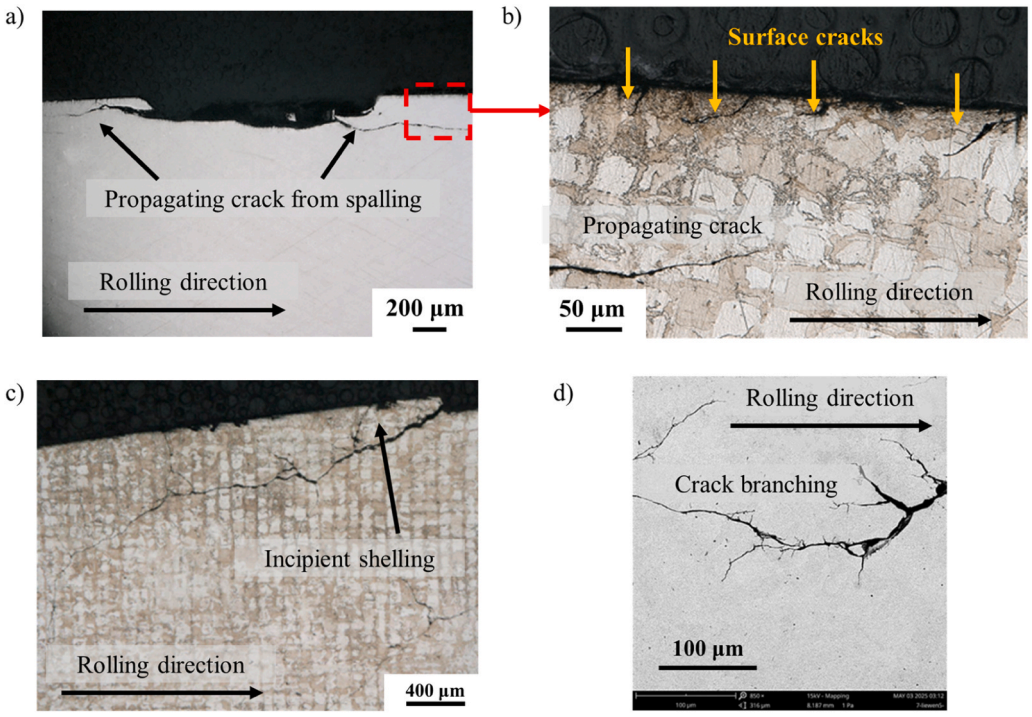

Fig. 3. Typical crack morphologies observed under rolling contact fatigue: a) Propagating crack from spalling (2000 MPa, oil); b) Surface cracks (2000 MPa, oil contaminant); c) Incipient shelling (1600 MPa, water); d) Crack branching (1400 MPa, water).

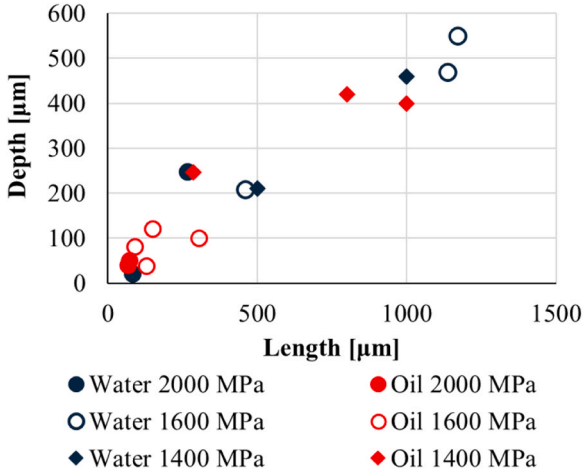

Fig. 4. Statistical distribution of cracks.

to isolate intrinsic crack-growth behaviour. In total, 15 such cracks were analysed.

Finite element simulations were conducted using the commercial software Abaqus® [22] to estimate the stress intensity factor in the rolling direction of significant cracks observed at the end of the test. Fig. 5a illustrates the model dimensions. The two contacting bodies were designed as a rectangle (representing the additive disc) and a circular sector representing the antagonist body. The bodies were modelled with plane strain elements. The lower edge of the rectangular body was fully constrained to the ground, while a reference point was applied at the centre of the circular sector. This reference point was connected to the upper part of the geometry through beam-type connectors to transmit motion.

The upper body was first placed in contact with the rectangle and subsequently translated from right to left to simulate a loading cycle. The applied forces in the models were 0.80 kN/mm, 1.05 kN/mm, and 1.63 kN/mm, corresponding to the Hertzian pressures experimentally applied. The constitutive behavior was assumed to be linear elastic, with a Young's modulus E of 210 GPa and a Poisson's ratio υ of 0.3 for both components. A general contact interaction was applied to the whole model and a friction equal to that experimentally estimated was applied (0.027 for oil lubricant, 0.013 for water lubricant). Quadratic CPE8R plane strain elements were applied to the model; the mesh size ranged from 1 mm in regions distant from contact to 0.01 mm near the crack tip and contact areas. A circular partition was applied at the crack tip to define the crack properties. Degenerate elements and the position of the degenerate nodes (quarter points) were specified, as they are necessary for the computation of stress intensity factors (SIFs) (Fig. 5b). The SIF values were calculated using the nodal displacement method in accordance with Williams' equations [23]:

$$K_I = (u_1 - u_2)\frac{E\sqrt{\frac{2\pi}{r}}}{8(1-\nu^2)} \tag{2}$$

$$K_{II} = (w_1 - w_2)\frac{E\sqrt{\frac{2\pi}{r}}}{8(1-\nu^2)} \tag{3}$$

where u_i and w_i represent the displacements of the quarter points at the crack tip, and r is the distance between the quarter point and the crack tip. Specifically, u_i corresponds to the Crack Opening Displacements (COD) in mode I, while w_i represents the Crack Shearing Displacements (COD) in mode II. Given the stress intensity factors range in mode I and mode II estimated from the finite element model, SIF range equivalent variation is estimated with the equation [2]:

$$\Delta K_{eq} = \sqrt{(1.43\Delta K_I)^2 + \Delta K_{II}{}^2} \tag{4}$$

It should be noted that ΔK_I was estimated considering only the positive component of the cycle, since the negative part does not contribute to crack propagation.

Fig. 6a and Fig. 6b show the variation of the stress intensity factors for mode I and mode II, ΔK_I and ΔK_{II}, as a function of the crack length L,

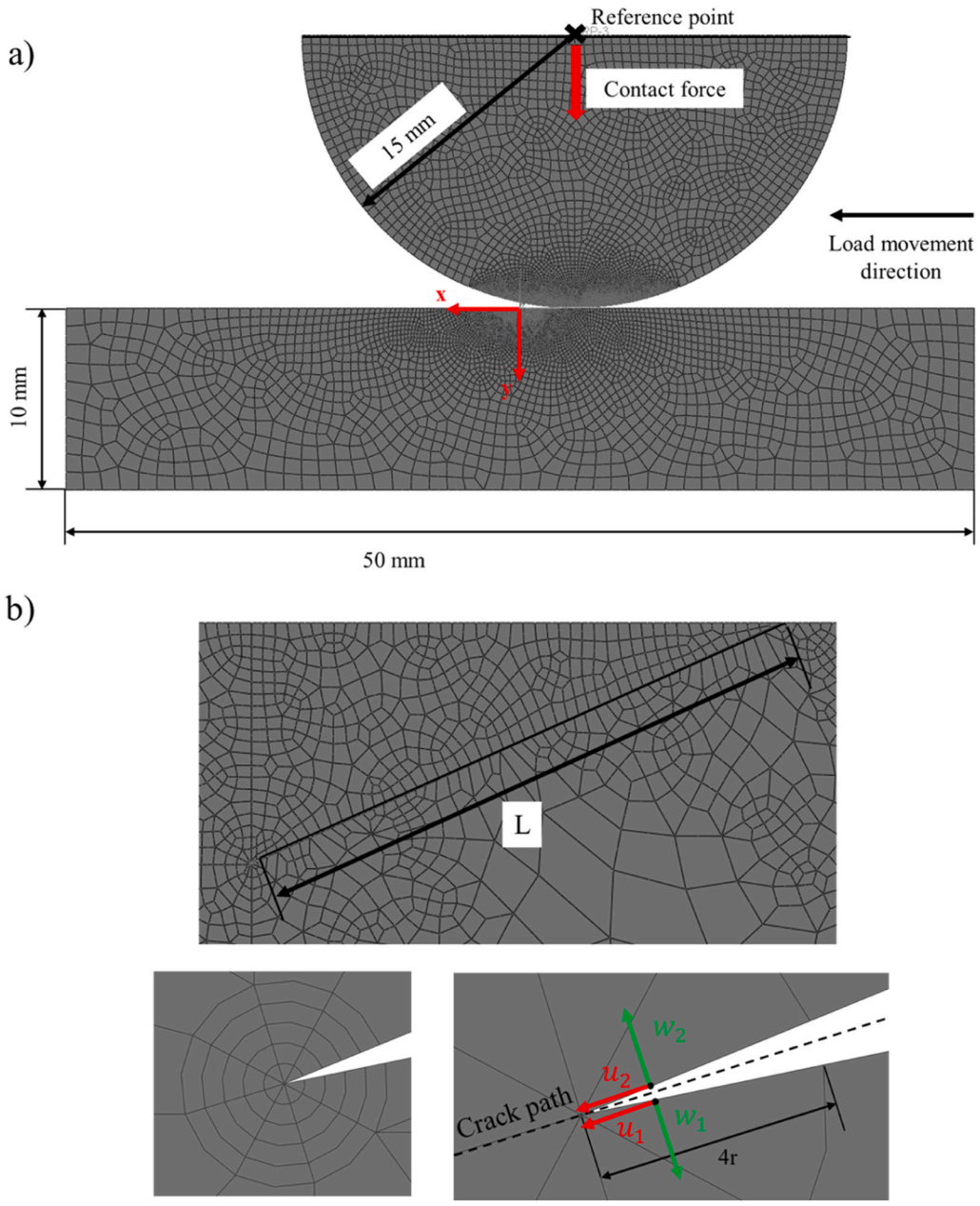

Fig. 5. Finite element model of the surface-cracked contact configuration. (a) General model assembly and boundary conditions; (b) detail of the surface crack geometry and definition of quarter-point elements used for stress intensity factor (SIF) calculation.

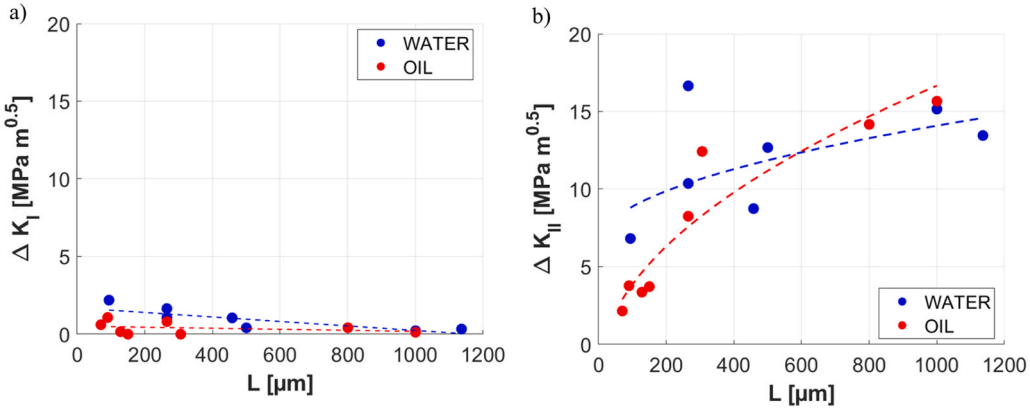

Fig. 6. a) Stress intensity factor range in mode I by varying crack length; b) Stress intensity factor range in mode II by varying crack length.

under water and oil contact conditions. The ΔK_I values are significantly lower than those of ΔK_{II} and become negligible as the crack length increases. Conversely, ΔK_{II} exhibits a clear increasing trend with L. The crack growth rate $\Delta a/\Delta N$ was estimated under the assumption that cracks nucleate from cycle zero, providing an approximation of early-stage fatigue behaviour. This assumption is consistent with the intrinsically cracked surface of the AM sample due to roughness. In particular, Δa was determined as the final crack length after sample failure, and ΔN as the number of cycles.

The mean crack growth rate can be expressed with the Paris law like equation:

$$\frac{\Delta a}{\Delta N} = C\,\Delta K_{eq}{}^{m} \tag{5}$$

where C and m are material coefficients. Fig. 7 summarizes the relationship between the effective stress intensity factor range and the measured crack growth rate under both lubrication regimes. Fig. 6a displays the Paris-law fits, revealing a markedly higher propagation rate in water-lubricated specimens, consistent with hydraulic pressurization and mixed-lubrication effects. Fig. 6b-d provide parity plots comparing experimental and model-predicted values. The global correlation in Fig. 6b confirms that the classical linear Paris formulation captures the general trend but exhibits considerable scatter, particularly for the water condition shown in Fig. 6c, where data deviate significantly from the ideal parity line. Conversely, oil-lubricated tests (Fig. 6d) display a slightly improved correlation, reflecting the more stable contact conditions ensured by the thicker lubricant film. Table 3 summarizes the coefficients C and m, together with the determination coefficient R^2, obtained from linear regressions on the complete dataset and on the subsets corresponding to water and oil conditions. The R^2 values indicate that the linear model explains only a moderate portion of the total variability ($R^2 = 0.31$) and performs very poorly for the water data ($R^2 = 0.06$), suggesting a weak or non-linear relationship. In the case of oil, the regression shows a slightly better fit ($R^2 = 0.42$), although still insufficient to reliably describe the experimental trend.

To overcome the limitations of the linear model and better capture the observed variability, a second predictive formulation, hereafter referred to as the GAMMA model, was developed to describe the crack growth behaviour in rolling contact fatigue conditions through the combined action of mechanical and tribological descriptors. This approach relies on the experimental evidence that RCF cracks started from surface; thus, tribological effects on crack growth rate must be more deeply considered. In this approach, the lubrication regime is represented by two dimensionless similarity parameters, Γ_I and Γ_{II}, defined as [24,25]:

$$\Gamma_I = G(2U)^{0.25} \tag{6}$$

$$\Gamma_{II} = W/(2U)^{0.5} \tag{7}$$

where

Table 3
Crack propagation law parameters obtained through calibration and respective R^2.

	C	m	R^2
Total	3.4751×10^{-10}	0.708	0.3142
Water	4.3237×10^{-10}	0.731	0.0616
Oil	4.3494×10^{-10}	0.457	0.4226

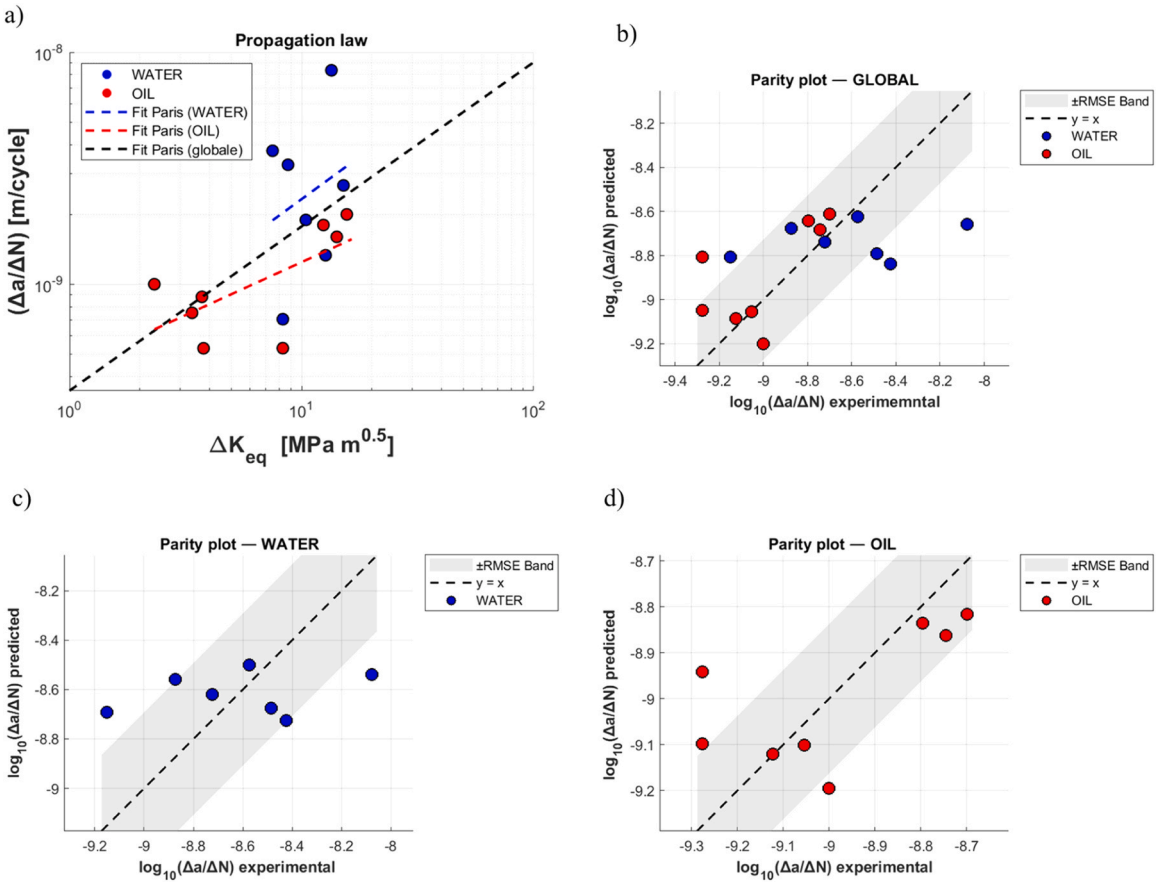

Fig. 7. Fatigue crack growth in WATER and OIL environments. (a) Crack growth rate ($\Delta a/\Delta N$)vs. effective stress intensity range ΔK_{eff} with Paris law fits for each environment. (b) Global parity plot comparing predicted and experimental growth rate. (c) Parity plot for WATER tests. (d) Parity plot for OIL tests.

$$G = \alpha_P E' \tag{8}$$

$$U = \frac{\eta u_m}{E' R_x} \tag{9}$$

$$W = \frac{F}{l E' R_x} \tag{10}$$

where η is the dynamic viscosity of the lubricant, u_m the average surface speed, R_x the equivalent roller radius, α the pressure–viscosity coefficient, w the Hertzian line load per unit length and E' the reduced modulus of elasticity [26]:

$$E' = \frac{E}{(1-\upsilon^2)} \tag{11}$$

These parameters compactly account for the effects of load, viscosity, geometry and speed on the overall lubrication state. Since the present configuration corresponds to a line contact, the similarity parameters Γ_I and Γ_{II} were evaluated using nominal Hertzian quantities and averaged across the contact width. In this way, both parameters describe the mean lubrication state representative of the entire contact zone rather than localized point values. This assumption is consistent with the quasi-uniform pressure and film thickness distribution along the contact line, and it allows for a direct comparison between different load and lubricant conditions within a unified framework. Both similarity parameters are interrelated, since the entrainment speed and the applied load jointly determine the local pressure and film-thickness evolution within the contact. An increase in lubricant viscosity affects the two parameters in opposite ways: it increases Γ_I through the entrainment parameter U (which grows with viscosity and enhances viscous transport into the contact), while it decreases Γ_{II} through the load parameter W (as a more stable full-film regime reduces asperity interaction). As a consequence, Γ_I and Γ_{II} cannot be considered fully independent, and the viscosity governs the balance between hydrodynamic support and asperity interaction, ultimately influencing the crack propagation rate predicted by the GAMMA formulation.

Table 4 shows the dynamic viscosity η_0 for the oil and water lubricants at atmospheric pressure and the pressure-viscosity coefficient α. The pressure-dependent effective viscosity coefficient η was estimated by the Roelands' equation [27]. The pressure-dependent effective viscosity η and the resulting EHL parameters for the tested conditions are summarised in Table 5.

The calculated parameters indicate that oil lubrication results in higher Γ_I values due to its greater viscosity and pressure–viscosity coefficient, reflecting a more stable full-film regime across all load levels. Conversely, the water–glycol lubricant exhibits higher Γ_{II} values owing to its lower entrainment parameter U, which shifts the contact toward mixed lubrication, where partial film breakdown and asperity interactions become more likely. The increase in Γ_{II} under water-based lubrication conditions is consistent with the experimentally observed intensification of surface damage and the accelerated crack propagation. These parameters were subsequently incorporated into the GAMMA formulation to quantify their combined influence on the crack growth rate.

The crack growth rate was expressed as a power law of the effective stress intensity factors and the two EHL parameters:

$$\frac{\Delta a}{\Delta N_{GAMMA}} = C\Delta K_{eq}^{a}\,\Gamma_I^{b}\Gamma_{II}^{c} \tag{12}$$

Table 4
Dynamic viscosity and pressure-viscosity coefficients for the oil and water contaminants.

Lubricant	η_0 [Pa s]	α [Pa^{-1}]
Oil	0.020	2.0×10^{-8}
Water	0.0015	1.2×10^{-8}

Table 5
Pressure-dependent effective viscosity and EHL similarity parameters for oil and water lubrication.

Lubricant	p_H [MPa]	η [MPa]	Γ_I	Γ_{II}
Oil	1400	1.68×10^{6}	982	0.005
Oil	1600	1.26×10^{7}	1623	0.002
Oil	2000	5.70×10^{8}	4213	0.001
Water	1400	2.13×10^{2}	62.5	0.406
Water	1600	8.44×10^{2}	88.2	0.290
Water	2000	1.19×10^{2}	171	0.122

Or, equivalently, in logarithmic form:

$$\log_{10}\frac{\Delta a}{\Delta N_{GAMMA}} = \log_{10} C + a\log_{10}\Delta K_{eq} + b\,\log_{10}\Gamma_I + c\,\log_{10}\Gamma_{II} \tag{13}$$

To estimate the regression coefficients, a multiple linear regression was performed in the log–log domain, using Leave-One-Out (LOO) cross-validation to assess model robustness. At each LOO iteration, the model was refitted excluding one observation, and the withheld data point was predicted to evaluate out-of-sample performance. This approach ensures that the model is not overfitted and that each parameter contributes consistently to the prediction of the crack growth rate. Table 6 shows the regression coefficients of the model. The resulting model in power-law form is:

$$\frac{\Delta a}{\Delta N_{GAMMA}} = 5.62 \times 10^{-21}\Delta K_{eq}^{\,1.031}\Gamma_I^{\,6.824}\Gamma_{II}^{\,4.263} \tag{14}$$

Fig. 8 presents the parity plot comparing the experimental and predicted values of the crack growth rate obtained from the model. Each marker corresponds to an individual test condition, the dashed line indicates the ideal correspondence between the predicted and the experimental, while the shaded regions represent uncertainty intervals: the inner grey band corresponds to ±RMSE. The data exhibit a strong linear correlation and limited dispersion, with about 75 % of the points lying within the ±RMSE envelope, confirming the model's high predictive accuracy and absence of systematic bias ($R^2 = 0.75$, RMSE = 0.195). Oil-lubricated specimens cluster toward the lower-left region of the plot, corresponding to lower crack growth rates, while water-lubricated ones occupy the upper-right region, reflecting enhanced shear and faster propagation under mixed or boundary lubrication.

The figure supports the physical validity and numerical stability of the formulation, demonstrating that the combined mechanical and tribological descriptors, ΔK_{eq}, Γ_I, and Γ_{II}, successfully capture the shear-driven dissipation mechanisms governing crack propagation in lubricated RCF conditions. The standard deviation of the coefficients ranges from 0.049 (for ΔK_{eq}) to about 0.176–0.231 (for Γ_{II} and Γ_I), corresponding to a relative variability of approximately 3–6 %. This indicates that all predictors contribute consistently across different data partitions and that the model is not dominated by individual samples, despite the limited dataset and potential collinearity between the two EHL descriptors. The positive exponents on both EHL similarity parameters confirm that tribological and viscous dissipation effects significantly accelerate the fatigue damage process: increased viscosity (or higher pressure-viscosity coefficient) raises Γ_I, enhancing shear stress within the lubricant film, whereas higher normal load and reduced speed raise Γ_{II}, intensifying asperity interactions. Both mechanisms act synergisti-

Table 6
Regression coefficients of the GAMMA model (mean ± standard deviation, log–log domain).

Predictor	$b_{mean} \pm \sigma_b$
Intercept b_0	−20.25 ± 0.464
$\log_{10}\Delta K_{eq}$	+ 1.031 ± 0.049
$\log_{10}\Gamma_I$	+ 6.824 ± 0.176
$\log_{10}\Gamma_{II}$	+ 4.263 ± 0.231

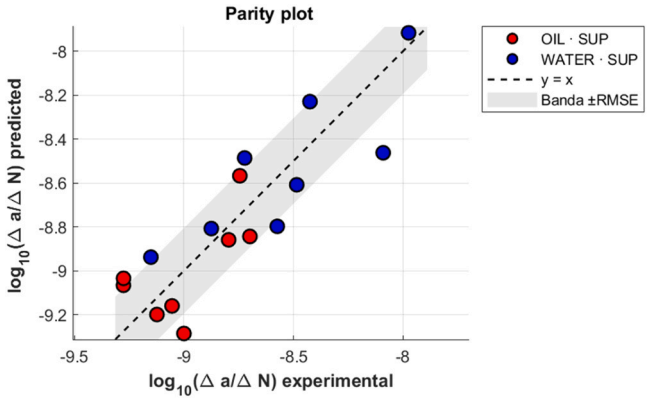

Fig. 8. Parity plot comparing experimental and predicted crack growth rates according to the GAMMA model.

cally with the cyclic stress intensity to produce localized shear and microcrack extension near the surface, consistent with previous observations in mixed and boundary lubrication regimes.

4. Life prediction

Following the crack propagation analysis, the FAD framework is used to estimate fatigue life under rolling contact, incorporating lubrication effects and finite-life considerations. The Failure Assessment Diagram (FAD) was adopted as the main analytical tool to assess the rolling contact fatigue (RCF) resistance of the investigated components. The FAD combines fracture mechanics concepts with fatigue criteria in a normalized diagram, providing a comprehensive framework that accounts for material properties, operating conditions, and the presence of inherent defects such as inclusions. In this approach, defects are treated as equivalent short cracks, following Murakami's theory [3], and structural integrity is evaluated in terms of their propagation or arrest under cyclic contact loading. The formulation originates from the El-Haddad short-crack model [4]:

$$\Delta K_{th} = \Delta K_{th,l.c.}\sqrt{\frac{a}{a+a_D}} \tag{15}$$

where ΔK_{th} is the threshold stress intensity factor (SIF) for a crack of length a, $\Delta K_{th,l.c.}$ the long-crack threshold SIF, and a_D the intrinsic crack length marking the transition between short- and long-crack regimes.

Normalized variables are defined as:

$$P_P = \frac{\mathrm{p}}{p_0} \tag{16}$$

$$K_P = \frac{\Delta K_{eq}}{\Delta K_{I,th,l.c.}} \tag{17}$$

where p_0 is the plane RCF pressure limit defined as:

$$p_0 = 1.102\sigma_{UTS} \tag{18}$$

The FAD limit curve is then given by:

$$K_P = \sqrt{1-P_P^2} \tag{19}$$

Eq. (19) defines the boundary between safe and unsafe conditions. Reference points representing specific loading and material states are plotted in the $P_P - K_P$ plane: if they lie below the curve, inherent cracks are arrested and the component is safe; if they lie above, cracks propagate and RCF failure is expected.

To extend the analysis to finite life, thresholds $\Delta\sigma_N$ and $\Delta K_{th,N}$ are expressed as cycle-dependent quantities:

$$\Delta\sigma_N = \Delta\sigma_\infty\left(\frac{N_\infty}{N}\right)^{\frac{1}{k}} \tag{20}$$

$$\Delta K_{th,N} = \Delta K_{th,l.c.}\left(\frac{N_\infty}{N}\right)^{\frac{1}{m}} \tag{21}$$

where $\Delta\sigma_N$ is the finite-life stress amplitude, $\Delta\sigma_\infty$ the infinite-life value, N the number of cycles to failure, N_∞ the knee-point cycles of the S–N curve, k the Basquin exponent, and m the Paris exponent.

The finite-life FAD takes the form:

$$\Delta K_{p,N} = \left(\frac{N_\infty}{N}\right)^{\frac{1}{m}}\sqrt{1-P_{p,N}^2\left(\frac{N_\infty}{N}\right)^{-\frac{2}{k}}} \tag{22}$$

Eq. (22) produces iso-life curves that evolve from the infinite-life circular boundary to elliptical shapes representing progressively shorter lives. m was calculated from the relationship proposed by Fleck et al. [28]:

$$m = \frac{4}{\log[K_{IC}(1-R)\,] - \log\Delta K_{th,l.c.}} \tag{23}$$

Additional damage mechanisms are included through specific boundaries:

$$\frac{\Delta K}{K_{IC}(1-R)} = 1 \tag{24}$$

$$p_{sh} = 4\tau_Y \ (f < 0.25) \tag{25}$$

Eq. (24) represents the static fracture limit, where K_{IC} is the fracture toughness and R the load ratio. Eq. (25) gives the ratcheting (shakedown) limit, where τ_Y is the shear yield stress and f the friction coefficient.

The complete diagram is therefore divided into distinct regions: a safe zone (infinite life), a defect-controlled RCF zone ($a > a_D$), a stress-controlled RCF zone ($a < a_D$), a ratcheting zone beyond the shakedown limit, and a static fracture zone above the toughness threshold. The position of the reference point relative to these zones provides a clear prediction of the expected failure mode and the corresponding fatigue life of the component.

The equivalent stress intensity factors ΔK_{eq} was estimated from the same finite element model described in the previous paragraph. In this case, to investigate the behaviour of an incipient crack, a surface crack inclined at 25° was modelled on the rectangular body, with a depth of $0.01b_H$, where b_H, denotes the half-contact width. The selected inclination corresponds to the angle typically associated with the maximum SIF range, whereas the crack depth was estimated using Tallian's equations [29], which is also supported by subsequent studies [30,31]. Notably, the resulting depth is consistent with the median valley depth of the material's surface roughness profile.

Table 7 reports the material properties used to design the failure assessment diagram. The ultimate tensile stress and the yield stress were taken from [17], the fracture toughness and long crack growth threshold values are taken from Yadollahi et al. [12], using specimens produced with the same manufacturing technology and process parameters

Table 7
Mechanical properties adopted in FAD model.

Material properties	
Ultimate tensile stress, σ_{UTS} [MPa]	1100
Yield stress, σ_Y [MPa]	900
Fracture toughness, K_{IC} [MPa$\sqrt{m}$]	50
Long crack growth threshold, $K_{I,th,l.c.}$ [MPa$\sqrt{m}$]	3.54
k [-]	8
m [-]	2.76

investigated in this paper; the Basquin parameter from [29]; the parameter m was estimated from Eq. (23).

The Failure Assessment Diagram presented in Fig. 9 summarizes the rolling contact fatigue assessment in normalized form, explicitly showing the influence of load level and lubrication. The coloured curves represent finite-life iso-life boundaries with the number of cycles numerically estimated from Eq. (22). The iso-life curve on the right of the coloured regions refers to water-contaminated tests, those on the left to oil-contaminated ones. Each family of curves (green for 1400 MPa, blue for 1600 MPa, red for 2000 MPa) corresponds to a specific applied Hertzian pressure, and the shaded regions enclose all the iso-curves lying between the experimentally measured number of cycles to failure in water and that in oil.

The filled squares refer to the results of the crack simulated with numerical simulations. The experimental points are located close to the iso-life curves corresponding to the water-lubricated condition for all three pressure levels, whereas at he highest pressure the point falls within the region between the water and oil iso-life curves. Fig. 10 compares the predicted and experimental fatigue lives under different lubrication conditions. The dashed line represents the ideal correlation ($N_{predicted} = N_{experimental}$). The predicted life $N_{\text{predicted}}$ was numerically evaluated from Eq. (22) by imposing the effective stress intensity range $\Delta K_{p,N}$ estimated with FEM and $P_{p,N}$. Data points corresponding to tests performed in water (blue) and in oil (red) show that the model provides a reasonable estimation of the experimental results, with a tendency to slightly underpredict the fatigue life, particularly under oil lubrication. This slight deviation observed for the oil condition can be physically interpreted in terms of the lubricant penetration capability. The higher viscosity of oil reduces its ability to reach the crack tip, limiting hydraulic pressurization and therefore slowing crack advance. As a result, the experimental lives under oil lubrication tend to be longer than those predicted by the model, which assumes comparable fluid infiltration for both lubricants. This effect highlights the protective role of incomplete fluid penetration in high-viscosity environments, where crack growth is dominated by mechanical rather than hydraulic driving forces.

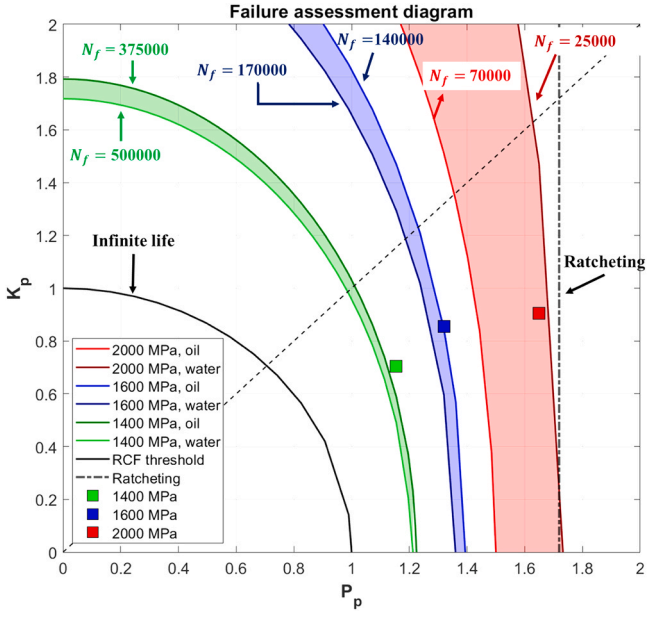

Fig. 9. Failure Assessment Diagram (FAD) for as-built L-PBF 17–4PH stainless steel under rolling contact fatigue. finite-life iso-life boundaries are shown for oil and water lubrication at Hertzian pressures of 1400, 1600, and 2000 MPa. Coloured bands represent the finite-life regions, while markers indicate the simulated reference points.

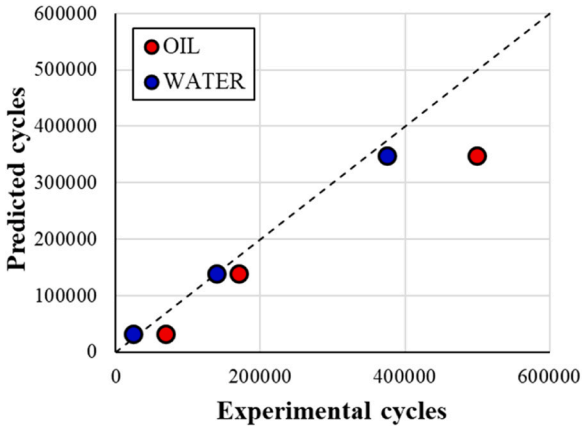

Fig. 10. Predicted versus experimental fatigue life under different lubrication regimes.

5. Conclusions

This work developed an extended Failure Assessment Diagram (FAD) framework for as-built L-PBF 17–4PH stainless steel, aimed at quantifying rolling contact fatigue (RCF) behaviour under different lubrication regimes. The study combined controlled twin-disc experiments, finite element analyses, and an analytical–empirical model to establish a unified methodology capable of linking lubrication conditions, stress intensity evolution, and fatigue life.

Finite element simulations were employed to evaluate the evolution of mode I and mode II stress intensity factors during rolling contact, providing the mechanical foundation for the analytical formulation. On this basis, the GAMMA model was introduced as a generalized crack-growth law incorporating both mechanical and tribological descriptors (ΔK_{eff}, Γ_I, Γ_{II}). The model achieved strong agreement with the experimental data ($R^2 = 0.75$, $RMSE = 0.195$), confirming its ability to capture the coupled influence of stress intensity, lubricant film characteristics, and viscous dissipation mechanisms on crack propagation kinetics.

The FAD approach was subsequently reformulated to include finite-life and lubrication-dependent parameters, enabling the delineation of safe, defect-controlled, and propagation regimes within a single normalized diagram. The resulting iso-life curves successfully reproduced the experimentally observed transitions between non-propagating and propagating conditions across the investigated pressure range and all loading conditions, with the model slightly underestimating the life in oil-lubricated tests. This behaviour reflects the conservative nature of the formulation and confirms its reliability in reproducing the observed trends under both lubrication regimes.

Overall, this study demonstrates that the integration of FEM-based stress analysis, lubrication-sensitive crack-growth modelling, and an extended FAD representation provides a robust, physics-informed framework for the assessment of RCF in additively manufactured steels. The methodology offers a practical foundation for defect-aware and lubrication-dependent design of AM components subjected to cyclic contact loading, bridging experimental observation and predictive fatigue modelling.

Future developments will aim to extend the present framework to heat-treated 17–4PH stainless steel and to mixed rolling–sliding conditions. This will enable the evaluation of how microstructural strengthening and tangential traction components affect the transition from crack initiation to propagation, thereby broadening the applicability of the model to real bearing and gear contacts.

CRediT authorship contribution statement

Candida Petrogalli: Writing – review & editing, Methodology, Conceptualization. **Kang Shu:** Writing – review & editing, Investigation. **Nicola Zani:** Writing – review & editing, Writing – original draft, Supervision, Resources, Methodology, Investigation, Data curation, Conceptualization. **Giorgio Donzella:** Writing – review & editing, Methodology, Investigation. **Angelo Mazzù:** Writing – review & editing, Methodology, Investigation.

Funding

The work was supported by the National Natural Science Foundation of China (No. 52405187).

Declaration of Competing Interest

The authors declare that they have no known competing financial interests or personal relationships that could have appeared to influence the work reported in this paper.

Data Availability

Data will be made available on request.

References

[1] Donzella G, Petrogalli C, Mazzù A. Application of a failure assessment diagram under rolling contact to components with hardness variable along the depth. Procedia Eng 2011;10:746–51. https://doi.org/10.1016/J.PROENG.2011.04.124.
[2] Donzella G, Petrogalli C. A failure assessment diagram for components subjected to rolling contact loading. Int J Fatigue 2010;32:256–68. https://doi.org/10.1016/J.IJFATIGUE.2009.06.016.
[3] Murakami Y, Endo M. Effects of defects, inclusions and inhomogeneities on fatigue strength. Int J Fatigue 1994;16:163–82. https://doi.org/10.1016/0142-1123(94)90001-9.
[4] El Haddad MH, Topper TH, Smith KN. Prediction of non propagating cracks. Eng Fract Mech 1979;11:573–84. https://doi.org/10.1016/0013-7944(79)90081-X.
[5] Donzella G, Faccoli M, Mazzù A, Petrogalli C, Roberti R. Progressive damage assessment in the near-surface layer of railway wheel-rail couple under cyclic contact. Wear 2011;271:408–16. https://doi.org/10.1016/j.wear.2010.10.042.
[6] Donzella G, Mazzù A, Petrogalli C. Failure assessment of subsurface rolling contact fatigue in surface hardened components. Eng Fract Mech 2013;103:26–38. https://doi.org/10.1016/J.ENGFRACMECH.2012.05.009.
[7] Herzog D, Seyda V, Wycisk E, Emmelmann C. Additive manufacturing of metals. Acta Mater 2016;117:371–92. https://doi.org/10.1016/j.actamat.2016.07.019.
[8] Becker TH, Kumar P, Ramamurty U. Fracture and fatigue in additively manufactured metals. Acta Mater 2021;219:117240. https://doi.org/10.1016/j.actamat.2021.117240.
[9] Liu H, Yu H, Guo C, Chen X, Zhong S, Zhou L, Osman A, Lu J. Review on fatigue of additive manufactured metallic alloys: microstructure, performance, enhancement, and assessment methods. Adv Mater 2024;36. https://doi.org/10.1002/adma.202306570.
[10] Murr LE, Martinez E, Hernandez J, Collins S, Amato KN, Gaytan SM, Shindo PW. Microstructures and properties of 17-4 PH stainless steel fabricated by selective laser melting. J Mater Res Technol 2012;1:167–77. https://doi.org/10.1016/S2238-7854(12)70029-7.
[11] Akita M, Uematsu Y, Kakiuchi T, Nakajima M, Kawaguchi R. Defect-dominated fatigue behavior in type 630 stainless steel fabricated by selective laser melting. Mater Sci Eng A 2016;666:19–26. https://doi.org/10.1016/j.msea.2016.04.042.
[12] Yadollahi A, Shamsaei N, Thompson SM, Elwany A, Bian L. Effects of building orientation and heat treatment on fatigue behavior of selective laser melted 17-4 PH stainless steel. Int J Fatigue 2017;94:218–35. https://doi.org/10.1016/j.ijfatigue.2016.03.014.
[13] Nezhadfar PD, Burford E, Anderson-Wedge K, Zhang B, Shao S, Daniewicz SR, Shamsaei N. Fatigue crack growth behavior of additively manufactured 17-4 PH stainless steel: Effects of build orientation and microstructure. Int J Fatigue 2019;123:168–79. https://doi.org/10.1016/j.ijfatigue.2019.02.015.
[14] Coors T, Faqiri MY, Saure F, Kahra C, Büdenbender C, Peddinghaus J, Prasanthan V, Pape F, Hassel T, Herbst S, Nürnberger F, Wester H, Uhe J, Breidenstein B, Denkena B, Behrens BA, Poll G, Maier HJ. Investigations on additively manufactured stainless bearings. Coatings 2022;12:1–20. https://doi.org/10.3390/coatings12111699.
[15] Basak AK, Ghasseb J, Pramanik A. Performance of gears manufactured through additive manufacturing. Metals (Basel) 2025;15. https://doi.org/10.3390/met15010063.
[16] Zhang Y, Daman AAA, He P, Li X, Borghesani P, Peng Z. Wear study of additively manufactured 316L stainless steel gears. Wear 2025:205796. https://doi.org/10.1016/J.WEAR.2025.205796.
[17] Zani N, Petrogalli C, Shu K, Cantaboni F, Ginestra PS. Rolling contact fatigue perspective of damage mechanism in 3D printed 17–4 PH stainless steel. Tribol Int 2025;211:110868. https://doi.org/10.1016/j.triboint.2025.110868.
[18] Morales-Espejel GE, Wainwright B, Kadiric A. Application of a contact fatigue life model to assess the relative risk of surface versus subsurface initiated fatigue in gears. Wear 578579 2025:206216. https://doi.org/10.1016/j.wear.2025.206216.
[19] Zani N, Petrogalli C, Battini D. Optimizing railway tribology: a systematic review and predictive modeling of twin-disc testing parameters. Lubricants 2024;12. https://doi.org/10.3390/lubricants12110382.
[20] Tandon N, Choudhury A. A review of vibration and acoustic measurement methods for the detection of defects in rolling element bearings. Tribol Int 1999;32:469–80. https://doi.org/10.1016/S0301-679X(99)00077-8.
[21] Igba J, Alemzadeh K, Durugbo C, Eiriksson ET. Analysing RMS and peak values of vibration signals for condition monitoring of wind turbine gearboxes. Renew Energy 2016;91:90–106. https://doi.org/10.1016/J.RENENE.2016.01.006.
[22] Abaqus, Abaqus Analysis User's Manual, Simulia, Providence, Rhode Island, 2020., (n.d.).
[23] Kuna M. Finite elements in fracture mechanic. s. Dordrecht: Springer Netherlands; 2013. https://doi.org/10.1007/978-94-007-6680-8.
[24] Hamrock BJ, Jacobson BO. Elastohydrodynamic lubrication of line contacts. A S L E Trans 1984;27:275–87. https://doi.org/10.1016/0043-1648(91)90325-O.
[25] Spikes HA. Sixty years of EHL. Lubr Sci 2006;18:265–91. https://doi.org/10.1002/LS.23.
[26] Johnson KL. Contact mechanics. Cambridge University press; 1985.
[27] C.J.A. Roelands, Correlational aspects of the viscosity-temperature-pressure relationship of lubricating oils, 1966. ⟨https://repository.tudelft.nl/record/uuid:1fb56839-9589-4ffb-98aa-4a20968d1f90⟩ (accessed November 6, 2025).
[28] Fleck NA, Kang KJ, Ashby MF. Overview no. 112: the cyclic properties of engineering materials. Acta Metall Mater 1994;42:365–81. https://doi.org/10.1016/0956-7151(94)90493-6.
[29] Tallian TE, Chiu YP, Van Amerongen E. Prediction of traction and microgeometry effects on rolling contact fatigue life. J Tribol 1978;100:156–65. https://doi.org/10.1115/1.3453127.
[30] Blake JW, Cheng HS. Surface pitting life model for spur gears. Part I. Life prediction. Am Soc Mech Eng 1990;113.
[31] Miller GR, Keer LM, Cheng HS. On the mechanics of fatigue crack growth due to contact loading. Proc R Soc Lond Ser A Math Phys Sci 1985;397. https://doi.org/10.1098/RSPA.1985.0011.